Boosting Ultrafast Lithium Storage Capability of Hierarchical Core/Shell Constructed Carbon Nanofiber/3D Interconnected Hybrid Network with Nanocarbon and FTO Nanoparticle Heterostructures

Bon-Ryul Koo, Ki-Wook Sung, and Hyo-Jin Ahn*

The aim of the study involves accelerating ultrafast electrochemical behavior of lithium-ion batteries (LIBs) by proposing hierarchical core/shell heterostructure of carbon nanofiber (CNF)/3D interconnected hybrid network with nanocarbon and fluorine-doped tin oxide (FTO) nanoparticles (NPs) via a one-pot process of horizontal ultrasonic spray pyrolysis deposition. This is constructed via a pyrolysis reaction of ketjen black forming 3D interconnected FTO NPs covered with nanocarbon network on CNF. It offers fast electrical conductivity to the overall electrode with improved Li ion diffusion due to decreased size effect and relaxed structural variation of FTO NPs via nanocarbon network, leading to high discharge capacity (868.7 mAh g^{-1} after 100 cycles) at 100 mA g^{-1} and superior rate capability. Nevertheless, at extremely high current density (2000 mA g^{-1}), significant ultrafast electrochemical performances with reversible discharge capacity (444.4 mAh g^{-1}) and long-term cycling retention (89.9% after 500 cycles) are noted. This is attributed to the novel effects of 3D interconnected hybrid network accelerating receptive capacity of Li ions into the FTO NPs via nanocarbon network, delivery of formed Li ions and electrons by hybrid network with FTO NP and nanocarbon, and prevention of FTO NP pulverization from CNFs via nanocarbon network. Therefore, the proposed heterostructure holds significant promise for effective development of ultrafast anode material for enhancing the practical applications of LIBs.

1. Introduction

Given the ever-increasing energy demands in high-power-driven applications (e.g., smart grids and electric vehicles), several studies have focused on upgrading and achieving efficient and fast energy storage ability with high-rate capability and good cycle retention in rechargeable lithium-ion batteries (LIBs), which is one of the most widely used power sources.[1,2] Given the scientific principle wherein the performances of LIBs depend on electrochemical characteristics of the electrode material used in the system, the ultrafast capability of commercial graphite used as representative anode material in LIBs presents limitations in terms of being implementable via adjective intercalation kinetics of Li ions due to occurrence of Li plating at a high current density.[3,4] A significant effort to satisfy the efficient performances of LIBs required from advanced applications involves discovering an alternative electrode material with high capacity and stability at ultrafast current densities. Among various alternatives, tin oxide (SnO_2) is a promising anode material for LIBs due to its higher theoretical lithium-storage capacity (1493.0 mAh g^{-1}) when compared to commercial graphite (372.0 mAh g^{-1}) along with other advantages of low cost and nontoxicity.[5–7] However, the high lithium storage capacity corresponds to the main factor that accompanies significant volume expansion of the SnO_2 structure, exceeding 300%, and considerable aggregation in SnO_2 particles during insertion/extraction of Li ions. This results in stress-induced SnO_2 pulverization to cut-off electric contact between the electrode material and current collector and thereby diminishing the capacity of the LIB cells.[8] Additionally, at the ultrafast current density, to achieve fast energy storage ability that occurs with rapid kinetic behavior of Li ions, the aforementioned problems are highly accelerated via the poor electrical conductivity of SnO_2. This is considered as the main obstacle in limiting practical implementation of competent rate capability and ultrafast cycling stability of LIB cells via the nonhomogeneity of electrochemical reaction on the overall electrode.[9]

To promote LIB performances using SnO_2, a frequently reported strategy involved constructing unique nanostructured morphologies including nanoparticles (NPs) with hollow and porous structures, nanorods, nanotubes, and nanosheets that can slightly improve rate performance via facilitating

B.-R. Koo, Prof. H.-J. Ahn
Program of Materials Science & Engineering
Convergence Institute of Biomedical Engineering and Biomaterials
Seoul National University of Science and Technology
Seoul 01811, South Korea
E-mail: hjahn@seoultech.ac.kr
K.-W. Sung, Prof. H.-J. Ahn
Department of Materials Science and Engineering
Seoul National University of Science and Technology
Seoul 01811, South Korea

transportation of Li ions and relaxing the mechanical strain induced at SnO_2 during the cycling process. However, this is insufficient to obtain satisfactory performances due to significant side reaction and aggregation at the nanostructure during the electrochemical reaction.[10–14] An effective strategy corresponds to the doping of heteroatoms into SnO_2, such as Zn^{2+}, Sb^{5+}, and F^-, wherein it is important to improve electrical conductivity and Li ion diffusion of the material itself by providing extra free electrons to improve the specific capacity and cycling stability.[15,16] Specifically, F^- to form F-doped SnO_2 (FTO) by substituting O^{2-} in SnO_2 is observed to be an efficient doping source for SnO_2 due to the similar ionic radius of F^- (0.133 nm) and O^{2-} (0.132 nm). The process can yield electrical conductivity of up to 1×10^3 S cm^{-1} along with the unique advantages of good thermal and chemical stabilities.[17] Hence, FTO is utilized in diverse applications, such as transparent conductors, photocatalysts, and solar cells, although there is a paucity of studies on LIBs.[18–20] Furthermore, a method to incorporate SnO_2 in carbon materials (graphene, carbon nanofiber (CNF), and carbon nanotube) is useful to improve structural stability and electrical conductivity of the nanocomposite. However, in order to maintain the cycling stability of LIBs, it is necessary to ensure a low ratio of SnO_2 used in nanocomposites, which can limit the realization of specific capacity.[21,22] The introduction of SnO_2 nanostructures on carbon materials via a followed synthetic process is reported as an effort to overcome this limitation. The approach can effectively yield a guarantee of high specific capacity for LIB cells while it also requires a protective buffer layer on SnO_2 to prevent their cycling stability as a simple core/shell structure. This can unfortunately act as a limiting factor for delivering the natural capacity of active materials at a high rate via the unimposing structured design of nanocomposite in conjunction with decreasing possibilities of adaptation to practical applications due to complex and multistep synthetic processes.[23,24] Therefore, we expect to design a new hybrid nanocomposite by using intrinsic advantage of FTO and carbon material based on an uncomplicated process to yield an outstanding performance for ultrafast LIBs. This can constitute a novel approach to address engineering issues with respect to boosting ultrafast lithium-storage capability in LIBs.

To resolve the aforementioned considerations and upgrade ultrafast LIB performance, we developed a unique hierarchical core/shell heterostructure wherein 3D interconnected hybrid network with nanocarbon and FTO NP is constructed on CNF using the one-pot process of horizontal ultrasonic spray pyrolysis deposition (HUSPD). This corresponds to an advanced synthetic approach beyond the basic mold wherein the HUSPD can only fabricate film nanostructures. Specifically, given the commercialization of the FTO substrate over the 4-generation size (730 × 920 mm), set up by the in-line system of the HUSPD, the proposed approach exhibits an abundant possibility to commence mass production. This type of hierarchical core/shell heterostructure exhibits synergistic advantages to accelerate and stabilize electrochemical behavior useful for ultrafast LIB performance. In the core/shell heterostructure, the 3D interconnected nanocarbon network can induce the abundant access of Li ions at the interfacial surface, accelerate the diffusion of Li ions and electrons at the overall electrode, and relax the pulverization of the FTO NPs as a result of

minimizing their volume expansion during repetitive ultrafast cycling process. Specifically, the 3D interconnected FTO NPs existing on CNF shorten the diffusion distance of Li ions and also activates efficient electrochemical reaction. Thus, the hierarchical core/shell heterostructure electrode exhibits stable rate capability and excellent specific capacity and long-term cycling retention at ultrafast current density (2000 mA g^{-1}).

2. Results and Discussion

Figure 1a depicts an interesting mechanism for one-pot synthesis wherein the 3D interconnected hybrid network is constructed with nanocarbon and FTO NP on the CNFs via the HUSPD. The FTO formation using the HUSPD is performed by solvent evaporation, solute condensation, and thermal decomposition of the precursor droplets formed from the ultrasonic atomizer in a reaction furnace. This is followed by the chemical reaction of $SnCl_4 + 2H_2O + NH_4F \rightarrow SnO_2:F + 3HCl + NH_4Cl + HF$, which is mainly utilized to develop a film nanostructure.[25,26] High wettability induced by electrostatic interaction of water-based droplets with hydrophilic glass substrate is the main reason for forming FTO films on glass substrate instead of the independent NPs.[27,28] Hence, as a unique approach to breaking an existing frame, we attempted to use CNFs with a hydrophilic nature as obtained by acid treatment using a mixture of nitric acid and hydrofluoric acid as a substrate for one-pot construction of the interlocked FTO NPs acting as the shell layer that resulted in a core/shell nanocomposite structure with CNF/FTO. The existence of the KBs in the precursor droplets during the HUSPD acted as a major source to form an interconnected nanocarbon network covering the FTO NPs. As shown in Figure 1a, when the precursor droplets correspond to a pyrolysis reaction to form the FTO NPs, the KBs can form phenolic groups by oxidizing them with acidic products, such as HCl and HF, which are formed by a pyrolysis reaction of the FTO[29] given an endothermic peak at 340–380 °C as shown in the DSC curve of FTO precursor solution with KB (see Figure S1 in the Supporting Information). The phenomenon is confirmed by the Fourier transform infrared (FTIR) result that exhibits an emitted absorption peak at 1580 cm^{-1} in the only product obtained by the heat-treating FTO precursor solution with KB at 400 °C (see Figure 1b). Given further processing of a pyrolysis reaction, the FTO NPs formed via the decomposition and oxidation of $Sn_2(OH)_2O$, as shown in the XRD result in Figure 1c, becomes aggregated toward the core region of the intermediate product by their shrinkage and crystallization to form the FTO NPs.[30,31] Simultaneously, phenolic groups located at the shell region can form nanocarbon as increased carbon–carbon bond by their reduction reaction as induced by oxidation of $Sn_2(OH)_2O$ (see C 1s XPS curves of Figure S2 in the Supporting Information). This causes the formation of the FTO NPs covered by the nanocarbon as clearly shown in the scanning electron microscopy (SEM) image of the product obtained at the exhaust of the HUSPD wherein crystallites are independently distributed in an organic matrix without aggregation between them (see Figure S3b in the Supporting Information) in contrast to the product fabricated with only the FTO precursor (see Figure S3a in the Supporting Information).
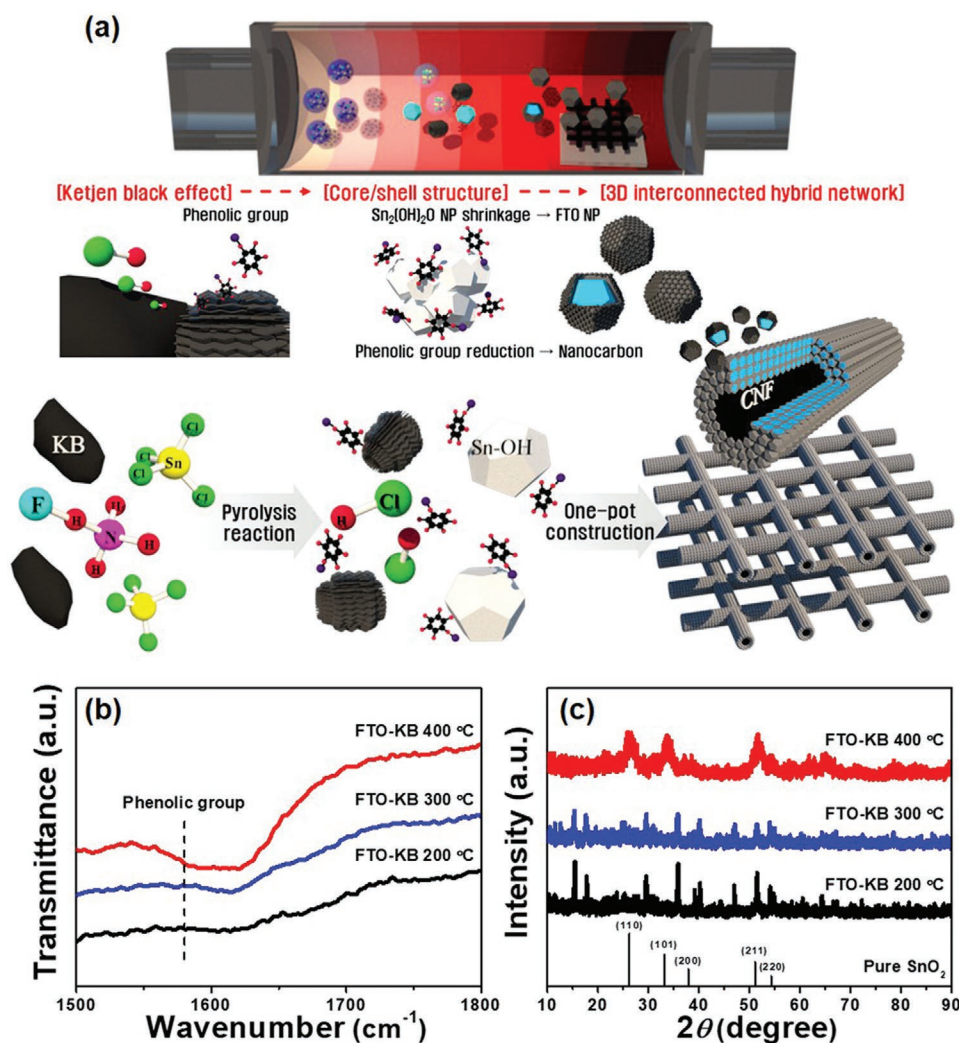
Figure 1. a) Schematic illustration of the one-pot construction process for 3D interconnected hybrid network with nanocarbon and FTO NP on CNF using the HUSPD b) FTIR and c) XRD curves of the products obtained by heat-treating FTO precursor solution with KB at 200, 300, and 400 °C.

Finally, by stacking nanocarbon-coated FTO NPs step-by-step on the CNFs, it is expected that the hierarchical core/shell heterostructure with CNF/3D interconnected hybrid network with nanocarbon and FTO NP is formed via the one-pot process of the HUSPD.

Figure 2a–c presents SEM images of bare CNF, CNF/FTO NP, and CNF/C-FTO NP, respectively. The bare CNF exhibits the smooth surface morphology of the 1D structure with a diameter range of 198.1–232.3 nm. However, the surfaces of CNF/FTO NP and CNF/C-FTO NP are densely covered by interlocked nanoparticles with an increased diameter ($\approx$291.9–327.0 nm for CNF/FTO NP and $\approx$301.1–318.8 nm for CNF/C-FTO NP) when compared to bare CNFs. This implies that the core/shell nanocomposite structure of CNF/FTO is elaborately formed by one-pot introduction of the FTO NPs on the CNF using the HUSPD. It is noted that the diameter and distribution of nanoparticles consisting of the shell of CNF/C-FTO NP are lower than those of CNF/FTO NP (see Figure 2d). This indicates that the shell layer of CNF/C-FTO NP is formed smoothly. The result is mainly attributed to the effect of KBs on FTO NPs

formed by HUSPD. Basic FTO deposition leads to preferential growth of the FTO grain to rod-shaped crystallites via their agglomeration[32,33] as a rough and sharp surface structure of the FTO deposited on glass substrate (Figure S4a, Supporting Information). Conversely, the use of KBs during FTO deposition can act as a major factor to suppress FTO agglomeration, and smoothing of surface structure on FTO films is generated with increases in the weight percentage of the KB (Figure S4b for 0.1 wt% KB and Figure S4c for 1 wt% KB in the Supporting Information) present in the FTO precursor solution. The smoother shell morphology of core/shell nanocomposite structure can favorably induce efficient electron transport during violent electrochemical reaction[33] as proved by the improved value of Hall mobility on the FTO films formed with increases in the weight percentage of KB (Figure S4d, in the Supporting Information). In the XRD results (Figure 2e), bare CNF reveals a broad diffraction peak at $\approx$24.00°, thereby corresponding to (002) plane of amorphous carbon. However, sharp emitting diffraction peaks are observed at 26.55°, 33.82°, 37.86°, and 51.73° for CNF/FTO NP and CNF/C-FTO NP in conjunction with
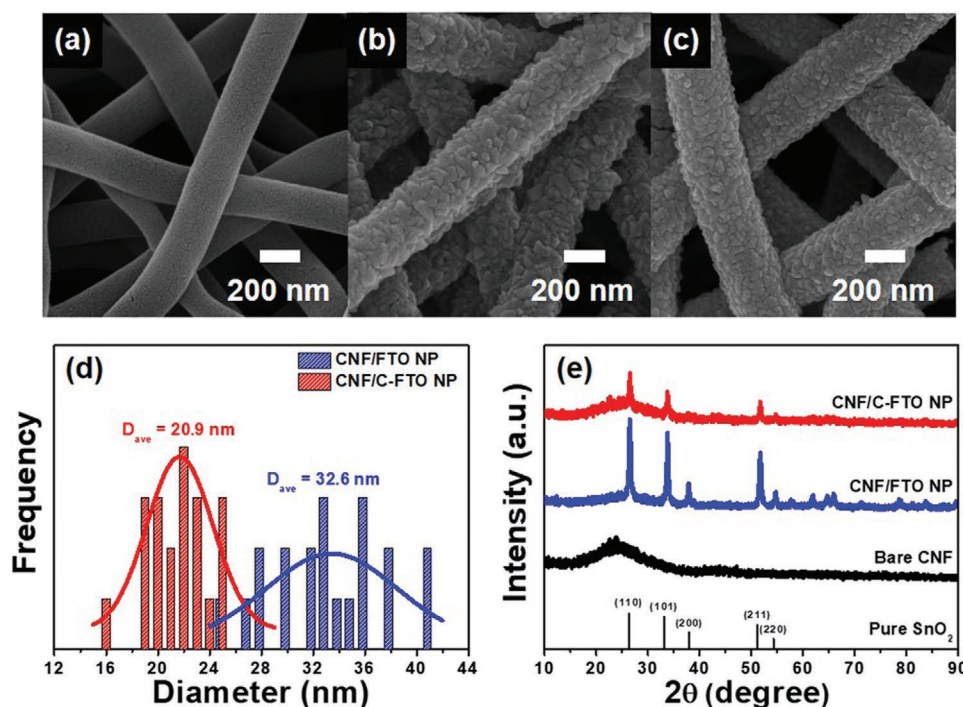
Figure 2. SEM images of a) bare CNF, b) CNF/FTO NP, and c) CNF/C-FTO NP; d) comparison in distribution of measured FTO NP diameters between CNF/FTO NP and CNF/C-FTO NP; e) XRD curves of bare CNF, CNF/FTO NP, and CNF/C-FTO NP.

weak diffraction peak related to amorphous carbon. This provides clear evidence of the formation of FTO phase with the (110), (101), (200), and (211) planes on the CNF as peak positions shift toward a slightly lower angle when compared to those of pure SnO_2 phase (26.61° for (110) plane, 33.90° for (101) plane, 37.98° for (200) plane, and 51.82° for (211) plane). Therefore, the result can indicate successful introduction of FTO NP as a shell layer on the CNF and can improve electrical conductivity of the overall electrode such that it is useful to accelerate ultrafast electrochemical performance by providing extra electrons as F^- with a relatively large ionic radius corresponding to 0.133 nm to substitute O^{2-} sites (ionic radius 0.132 nm) of SnO_2.[34,35] Additionally, with respect to CNF/C-FTO NP, the intensity of FTO diffraction peaks is significantly weaker than those of CNF/FTO NP. This implies the emergence of nanocarbon formed by KBs to decrease the relative amount of FTO NP in the shell layer. This can act as an excellent media for the ultrafast electrochemical reaction for LIBs with SnO_2-based active material.

We performed the transmission electron microscopy (TEM) analysis to clearly characterize the morphology and interstructure of the samples. In TEM images of **Figure 3**a,d, bare CNF exhibits a continuous 1D fibrous structure with smooth surface and diameter range of ≈213.3–219.3 nm. Following the HUSPD, it is observed that the dense layer interlocked with the nanoparticles is formed along the surface of the 1D fibrous structure. This indicates the complete core/shell nanocomposite structure with a diameter of ≈298.3−315.6 nm for CNF/FTO NP (Figure 3b) and ≈299.6−314.4 nm for CNF/C-FTO NP (Figure 3c), which is consistent with the FESEM results. Significantly, the high-resolution (HR) image of CNF/C-FTO NP (Figure 3f) reveals the existence of nanocarbon network that

completely covers the nanoparticles at the shell layer while it only consists of nanoparticles for CNF/FTO NP (Figure 3e). Figure 3g confirms the structure with FTO nanoparticles corresponding to the (200) plane of FTO based on a clear lattice fringe of 0.24 nm and amorphous nanocarbon network with a thickness of 2–3 nm as a clear and typical lamellar structure.[36] Additionally, elemental mapping of CNF/C-FTO NP (see Figure 3h) indicates that a distinct distribution of the C element exists at core and shell parts in the structure while Sn, O, and F elements are uniformly distributed on the entire area of the 1D structure. The results indicate the successful formation of the hierarchical core/shell heterostructure achieved by the 3D interconnected FTO NPs with nanocarbon network on the CNF. This causes the increased electrical conductivity of the overall electrode and a stable structure to simultaneously prevent the volumetric variation in FTO NPs during charge/discharge processes, and thus it is expected that ultrafast electrochemical performances will be effectively improved.[34,36]

The XPS analysis is utilized to prove chemical bonding state of bare CNF, CNF/FTO NP, and CNF/C-FTO NP. In Sn 3d XPS spectra of **Figure 4**a, CNF/FTO NP and CNF/C-FTO NP reveal two characteristic peaks approximately corresponding to 486.7 and 487.7 eV for Sn $3d_{5/2}$ and 495.2 and 496.3 eV for Sn $3d_{3/2}$. This corresponds to the binding energy of Sn–Sn of ≈486.7 and 495.2 eV and of Sn–F corresponding to ≈487.7 and 496.3 eV related to the F-doping effect into SnO_2 with F atomic percentage of 2.51 at% for CNF/FTO NP and 2.53 at% for CNF/C-FTO NP.[37,38] However, a related characteristic peak is not observed on bare CNF. Additionally, it is noted that the peak intensity of CNF/C-FTO NP is lower than that of CNF/FTO NP, which is due to the decrease in the relative amount of
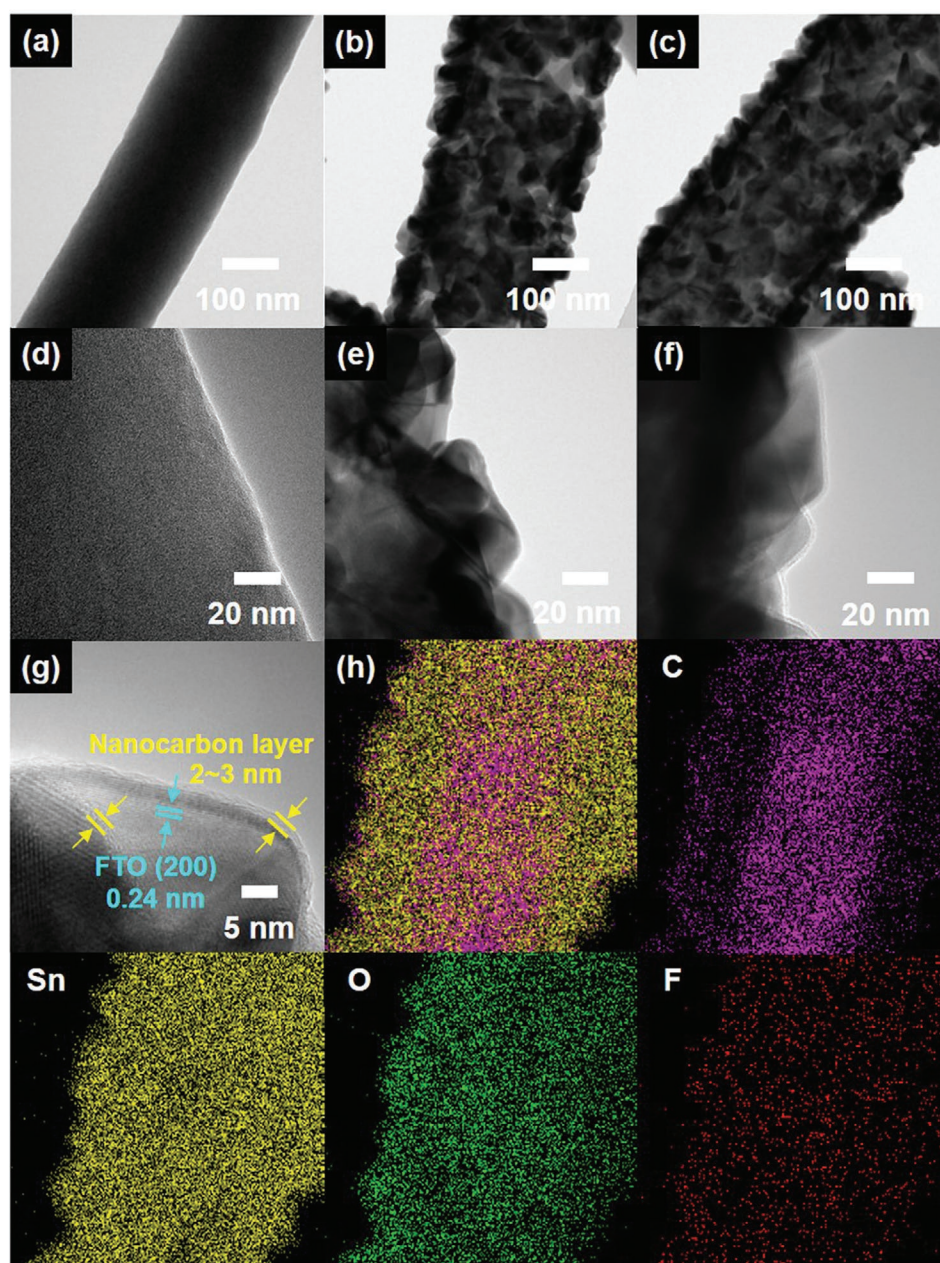
Figure 3. a–c) Low-resolution and d–f) high-resolution TEM images of bare CNF, CNF/FTO NP, and CNF/C-FTO NP, respectively, g) magnified HRTEM image of CNF/C-FTO NP, and h) elemental mapping of C, Sn, O, and F elements in CNF/C-FTO NP.

the FTO NPs at the sample surface by the existence of a nanocarbon network. At O 1s, XPS spectra resolved into three characteristic peaks to correspond to C=O for ≈530.3 eV, Sn−O for ≈530.8 eV, and C−O for ≈532.2 eV[38] (see Figure 4b). However, the CNF/FTO NP exhibits major peak of Sn−O via the existence of FTO coating layer at the shell area in conjunction with miner peaks of C=O and C−O by the CNF positioned at the core area. With respect to CNF/C-FTO NP, the Sn−O peak is weakened and the C−O peak evidently becomes dominant. This corresponds to the accompanied effect of nanocarbon network that exists around the FTO NPs, which can favor transport of Li ions and electrons and structural stability of the FTO NPs during

the electrochemical reaction.[39] The structure of nanocarbon network is confirmed via the Raman measurement of the samples. As shown in the Raman spectra of Figure 4c, emission of two characteristic peaks exists at 1348 and 1583 cm^{-1} to indicate the disordered (D) band and graphite (G) band, respectively. The intensity ratio (I_D/I_G) of D and G bands is commonly used as a criterion for the degree of disorder of carbon materials,[39] and the calculated ratio is obtained as 1.03 for bare CNF, 0.99 for CNF/FTO NP, and 1.04 for CNF/C-FTO NP. The result indicates that the CNF at core area and nanocarbon network at shell area consisted of the amorphous structure. Furthermore, we investigated the mass content of composed materials in the
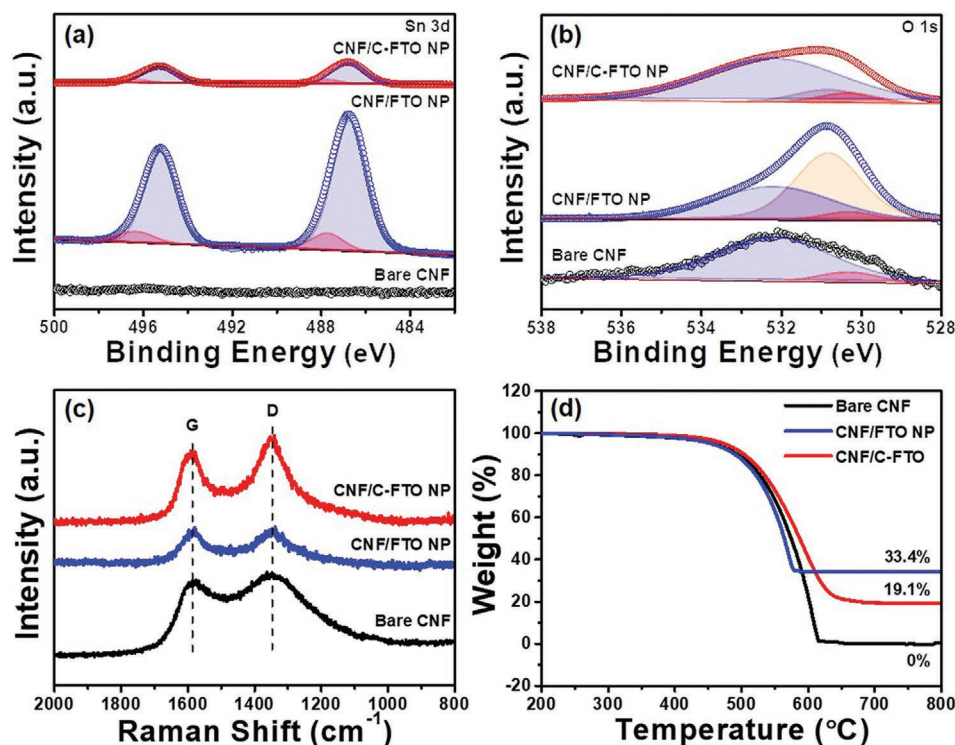
Figure 4. XPS spectra of a) Sn 3d and b) O 1s, c) Raman spectra, and d) TGA curve measured from 200 to 800 °C in air for bare CNF, CNF/FTO NP, and CNF/C-FTO NP.

core/shell nanocomposite using the TGA (see Figure 4d). When the temperature increases to 800 °C, the remaining weight corresponds to 0% for bare CNF, 33.4% for CNF/FTO NP, and 19.1% for CNF/C-FTO NP due to the burning of carbon materials. This indicates that the mass content of CNF, FTO, and nanocarbon network in the core/shell heterostructure (CNF/C-FTO NP) corresponds to 66.6%, 19.1%, and 14.3%, respectively.

Figure 5a,b shows the galvanostatic charge/discharge voltage profiles of CNF/FTO NP and CNF/C-FTO NP electrodes, respectively, as measured at the current density of 100 mA g^{-1}. Increased discharge capacity (1459.3 mAh g^{-1}) is observed at the first cycle of CNF/FTO NP electrode when compared to that (1353.2 mAh g^{-1}) of the CNF/C-FTO NP electrode. This is attributed to the weight ratio of the FTO NPs (33.4% for CNF/FTO NP and 19.1% for CNF/C-FTO NP) that consists of active materials, as shown in TGA results (Figure 4d). Specifically, the discharge capacity of CNF/FTO NP electrode exceeds that of pure SnO$_2$ NP-coated CNF electrode (1064.6 mAh g^{-1}) because F doping in SnO$_2$ can improve the electrical conductivity due to extra electrons to decrease the reactive energy barrier for the insertion of Li ions (Figure S5, Supporting Information).[40] The profile of two electrodes commonly indicates a voltage plateau at 0.8 V in the first cycle of the discharge process, which is mainly attributed to the reactions of lithiated SnO$_2$ (SnO$_2$ + 4Li$^+$ + 4e$^-$ → 2Li$_2$O + Sn) and SEI formation at active materials that produces irreversible capacity loss and the following decrease in Coulombic efficiency (41.3% for bare CNF electrode, 52.5% for CNF/FTO NP electrode, and 53.2% for CNF/C-FTO NP electrode). Additionally, the voltage plateau is identified at 0.30 V for the discharge process/0.70 V for the

charge process and 0.85 V for the discharge process/1.25 V for the charge process indicates Li–Sn alloying/dealloying (Sn + xLi$^+$ + xe$^-$ ↔ Li$_x$Sn (0 ≤ x ≤ 4.4)) and lithiation/delithiation of CNF (C + xLi$^+$ + xe$^-$ ↔ Li$_x$C), respectively, in conjunction with minor peak of 1.80 V related to the conversion of Sn into SnO$_2$, namely, the reversible redox reaction.[41] This induces the recovery of Coulombic efficiency above 95% after 10 cycles. Given the second cycle, the decreasing ratio of charge and discharge capacities for CNF/C-FTO NP electrode is less than that of CNF/FTO NP electrode. This increases the value of charge and discharge capacities at 10 cycles for CNF/C-FTO NP electrode, which can indicate to require some time of electrode activation for permeating electrolyte inside the active materials positioned at inner regions (the inner FTO and CNF) because the electrolyte may not have been contacted with the inner active materials at first due to nanocarbon network.[42–44] Thus, CNF/C-FTO NP electrode delivers a discharge capacity of 868.7 mAh g^{-1} at the 100th cycle and corresponding capacity retention of 95.2%, which exhibits an excellent performance when compared to CNF/FTO NP electrode that exhibits a discharge capacity of 465.1 mAh g^{-1} and capacity retention of 54.4% (see Figure 5c). The performance improvement can be due to the effect of 3D interconnected nanocarbon network to alleviate structural variation of FTO NPs with high specific capacity during cycling. Furthermore, in Figure 5d, CNF/C-FTO NP electrode evidently exhibits a superior rate capability at the accelerated current densities from 100 to 2000 mA g^{-1} and desirable capacity recovery when the current density returns to 100 mA g^{-1} when compared with performance of the CNF/FTO NP electrode. The resultant specific capacity at 2000 mA g^{-1} is
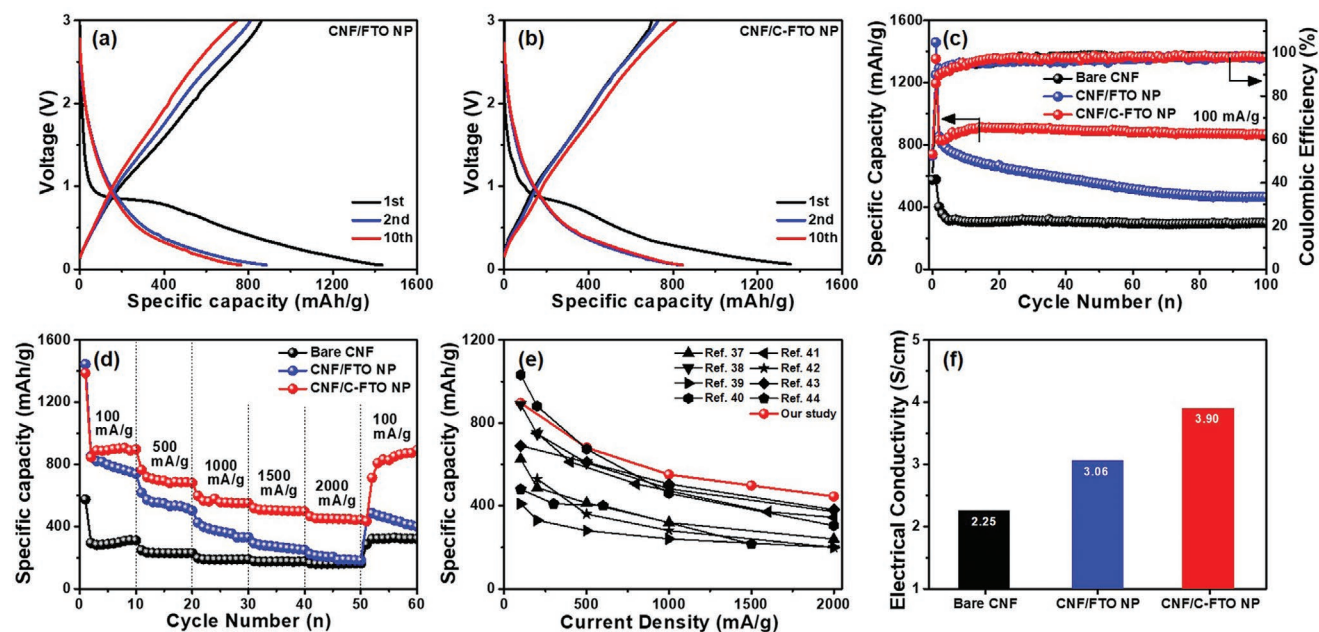
Figure 5. Galvanostatic charge/discharge voltage profiles of a) CNF/FTO NP and b) CNF/C-FTO NP electrodes measured at current density of 100 mA g^{-1}, c) cycle performance and d) rate capability of bare CNF, CNF/FTO NP, and CNF/C-FTO NP electrodes, e) comparative plot of the rate capability on CNF/C-FTO NP electrodes with previously-reported SnO$_2$-based composite electrodes for LIBs, and f) electrical conductivity measured from bare CNF, CNF/FTO NP, and CNF/C-FTO NP electrodes.

considered as a high standard when compared with previously reported SnO$_2$-based composites (see Figure 5e).[45–52] This is due to the improved diffusion coefficient of Li ions that is caused by the decreased size of FTO NPs to reduce diffusion pathway of formed Li ions in active material (see Figure S6 in the Supporting Information) and increased electron conductivity of overall electrode via the introduction of 3D interconnected hybrid network with nanocarbon and FTO NP on CNF (see Figure 5f).

The evaluation of ultrafast cycling capability on active materials for LIBs is an important factor given its applicability to practical products. **Figure 6**a exhibits the comparison in the ultrafast cycling capability of electrodes as measured by exposing the assembled cells at a general current density of 100 mA g^{-1} until 10 cycles and then an ultrafast current density corresponding to 2000 mA g^{-1} until 500 cycles. After 500 cycles, the CNF/C-FTO NP electrode maintains a significant value of 444.4 mAh g^{-1} (89.9% for cycling retention) despite the ultrafast current density of 2000 mA g^{-1} while the discharge capacities of bare CNF and CNF/FTO NP electrodes considerably decay to 105.7 and 175.8 mAh g^{-1}, respectively. The uneven performance of CNF/C-FTO NP electrode when compared to others can be generated via a unique impact to accelerate and stabilize ultrafast electrochemical behavior by the 3D interconnected hybrid network with nanocarbon and FTO NP on the CNFs. As shown in the schematic in Figure 6b, the 3D interconnected nanocarbon network can be used as an efficient accepter for Li ions at the interfacial surface, and this leads to the significant access of Li ions via ultrafast current density as suggested in the evidence presented in the increased specific surface area of CNF/C-FTO NP when compared to others (see **Figure 7**a). This can efficiently improve the desirable receptive capacity

of Li ions in the FTO NPs with significant capacity during the ultrafast electrochemical reaction. Additionally, when compared to other samples, CNF/C-FTO NP electrode exhibits excellent electrochemical kinetic properties via representing decreased charge transfer resistance (R_{ct}) and fasted Li-ion diffusion (see Figure S6 in the Supporting Information) as reflected from the smaller semicircle in the high medium-frequency region and increased angle of inclined line at low-frequency region (as the so-called Warburg impedance, Z_W), respectively, in the electrochemical impedance spectroscopy (EIS) spectra (see Figure 7b). This is attributed to the unique effect of FTO NP and nanocarbon in the 3D interconnected network structure to fulfill an efficient channel to transport Li ions and electrons. This developed the electrical conductivity of overall electrode such that is useful for improving ultrafast electrochemical reaction kinetics. As the recent attempt, the capacity contribution of Sn-based materials is characterized by two ways distinguishing specific electrochemical lithium-ion storage mechanisms; one is that conversion and alloying reactions are taken into account and another is to consider ion diffusion and surface induced capacitance.[53–56] Among these, in order to clearly confirm synergistic effect of the 3D interconnected hybrid network on CNF on lithium storage behavior at ultrafast electrochemical reaction, we calculated the degree of capacitive effect of the electrodes using the relationship between measured current (i) and scan rate (v) of the CV curves ($i = av^b$, where a and b are constants). The b value determined from the gradient of log i–log v plot is in the range between 0.5 and 1.0, which indicates that for a diffusion-controlled behavior b is close to 0.5, but for a capacitance-controlled process it approaches 1.0.[55–58] As shown in Figure S8 (Supporting Information), it is noted that the b value of CNF/C-FTO NP electrode is higher than that
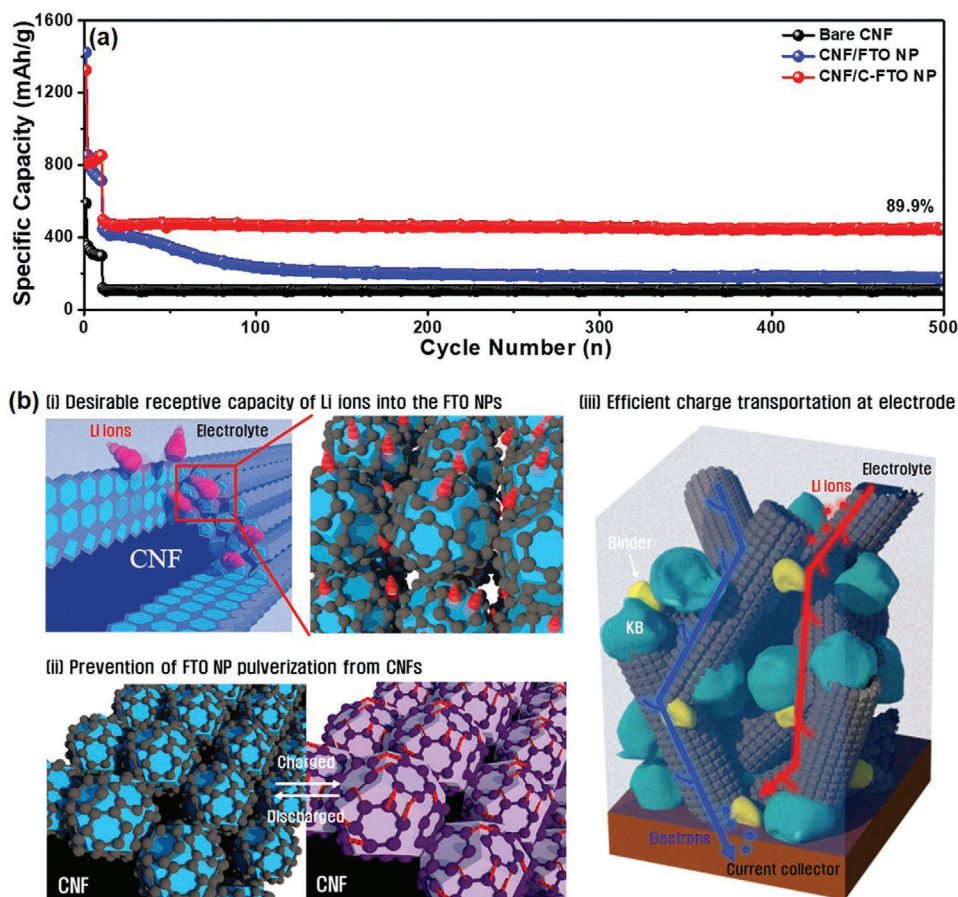
**ADVANCED
SCIENCE NEWS**
www.advancedsciencenews.com

**ADVANCED
FUNCTIONAL
MATERIALS**
www.afm-journal.de

Figure 6. a) Ultrafast cycling capability of bare CNF, CNF/FTO NP, and CNF/C-FTO NP electrodes measured at the current density of 2000 mA g^{-1} during 500 cycles and b) the schemed mechanisms to improve ultrafast cycling capability on CNF/C-FTO NP electrodes.

of CNF/FTO NP, which can indicate to have a more favored capacitive kinetics for CNF/C-FTO NP electrode.[59–62] This result can be attributed to efficient transportation of formed Li ions and electrons via the hybrid network consisting of FTO NP to provide fasted electrical conductivity and shorted diffusion pathway and nanocarbon to improve specific surface area in the nanocomposites. We also performed the quantification of ion diffusion and surface induced capacitance using the CV curves obtained at various scan rates (v) corresponding to 5, 10, 20, and 30 mV s^{-1}. As shown in Figure 7c, the CV curve of CNF/C-FTO NP electrode can be separated to two parts including the surface induced capacitance (pseudocapacitive, k_1v) and ion diffusion ($k_2v^{1/2}$) as given in the following equation (Equation (1))[63,64]

$$i(V) = k_1 v + k_2 v^{1/2} \tag{1}$$

Based on calculation results of CNF/FTO NP and CNF/C-FTO NP electrodes shown in Figure 7d, pseudocapacitive contribution gradually expands with increases in the scan rate. This indicates that pseudocapacitive mechanism based on insertion/extraction of Li ions is an important factor in the capacity of the nanocomposite. Interestingly, a higher pseudocapacitive contribution exists at overall scan rates on the CNF/C-FTO NP electrode when

compared to that of CNF/FTO NP electrode. This indicates that 3D interconnected hybrid network with nanocarbon and FTO NP on CNF is attributed to a useful electrochemical double-reaction with Li ions and electrons as synergistic effects to lead to the efficient receptive capacity of Li ions into FTO NPs and pathway for the delivery of Li ions and electrons to the current collector. This resulted in the excellent specific capacity at ultrafast current density. The excellent cyclic retention of CNF/C-FTO NP at the ultrafast electrochemical reaction is clearly observed as realized by comparing the structural variation of the electrode materials after 500 cycles (ultrafast current density of 2000 mA g^{-1}) as detected by the HRTEM. As shown in **Figure 8**a, the CNF/FTO NP electrode generates cracks throughout the surface, which can be induced by the ignorant volume expansion of the FTO NPs. This results in their exfoliation from the CNF following ultrafast electrochemical reactions (see Figure 8b). Conversely, the surface of CNF/C-FTO NP electrode remains smooth without any cracks as shown in Figure 8d. This indicates that the 3D interconnected nanocarbon network prevents pulverization of the FTO NPs (see Figure 8e) as with constant lattice fringe corresponding to 0.26 nm that is adjacent to that (0.24 nm, see Figure 8f) of pure FTO NP although significant variation in the lattice fringe exists on CNF/FTO NP (0.28 nm, see Figure 8c), keeping R_{ct} and Li-ion diffusion without critical degradation as shown in EIS
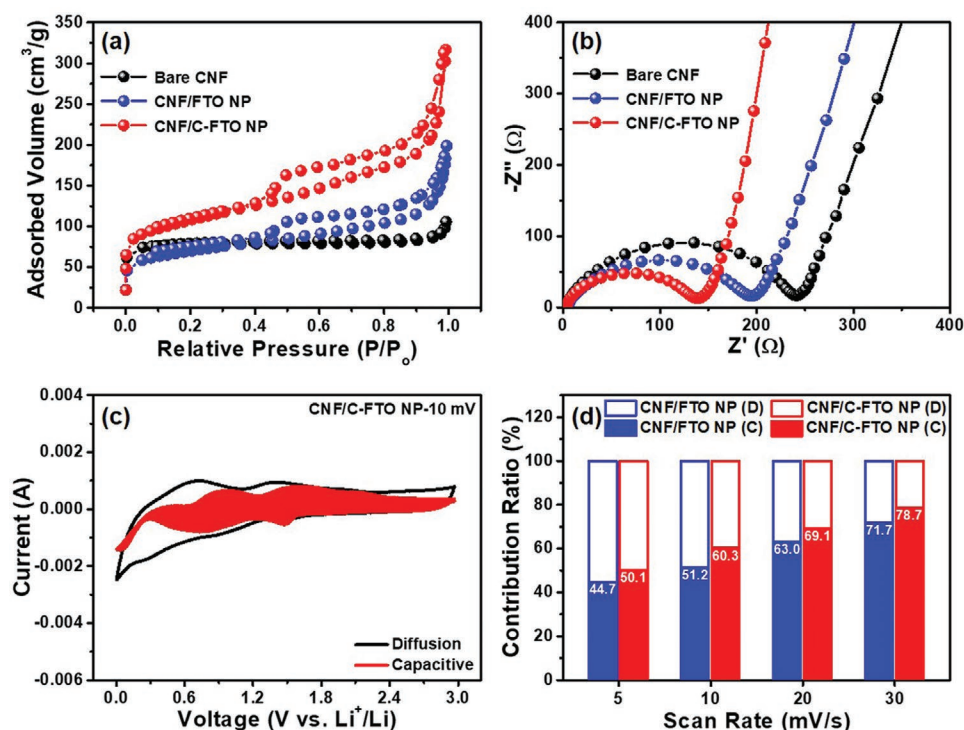
Figure 7. a) N_2 adsorption/desorption isotherms and b) Nyquist plots in the frequency range at the open-circuit potential obtained from bare CNF, CNF/FTO NP, and CNF/C-FTO NP electrodes, c) CV curve of CNF/C-FTO NP electrode with separation to diffusion current for vacant region and capacitive current for filled region at 10 mV s⁻¹, and d) the area comparison of diffusion (D) and capacitive (C) contributions between CNF/FTO NP and CNF/C-FTO NP electrodes with different scan rates.

spectra of the cell with CNF/C-FTO NP electrode after 500 cycles finished (see Figure S7 in the Supporting Information). Thus, one-pot construction of 3D interconnected hybrid network with nanocarbon and FTO NP on CNF can constitute a novel preposterous approach to provide excellent ultrafast electrochemical performances for future-oriented LIBs.
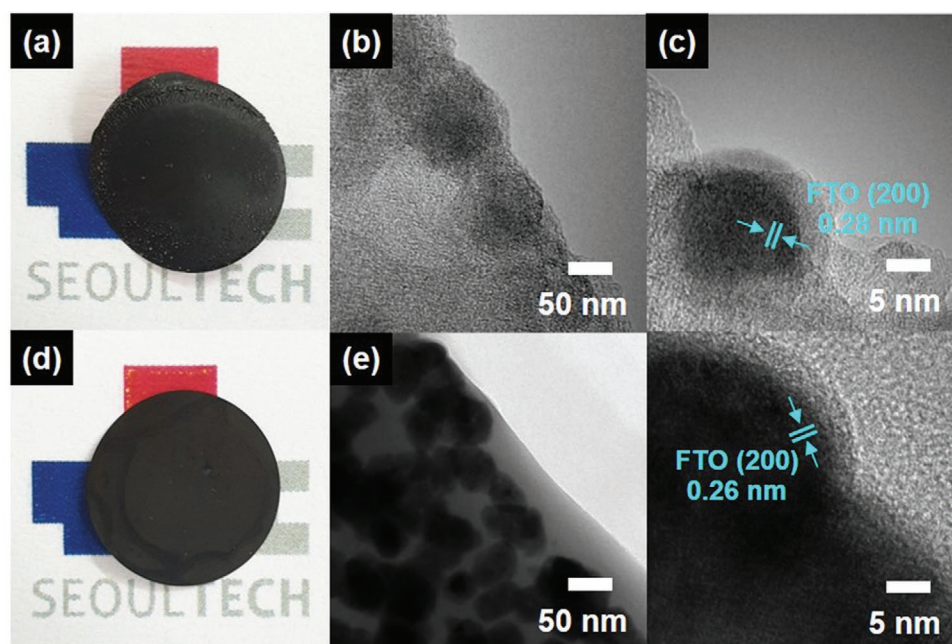

Figure 8. a,d) Actual photos, b,d) HRTEM images, and c,e) magnified HRTEM image of CNF/FTO NP and CNF/C-FTO NP electrodes after 500th cycles at 2000 mA g⁻¹, respectively.

3. Conclusions

In summary, we developed a unique hierarchical core/shell heterostructure of CNF/3D interconnected hybrid network with nanocarbon and FTO NP via one-pot construction of HUSPD that corresponds to an advanced synthetic route to surpass the current technical framework. During the HUSPD, the phenolic groups obtained from oxidation of KBs existent with FTO precursors served as a main source to form nanocarbon, and $Sn_2(OH)_2O$ was oxidized via shrinkage and crystallization to form FTO NPs. Hence, the 3D interconnected hybrid network was constructed on the CNFs with the stacking of formed nanocarbon-coated FTO NPs in a step-by-step manner. Thus, the 3D interconnected hybrid network with nanocarbon and FTO NP accelerated overall intrinsic electrical conductivity of the electrode. This was because the FTO NPs with decreased size increased the diffusion coefficient of Li ions and nanocarbon network and prevented the structural variation in the FTO NPs. This led to the competitive discharge capacity (868.7 mAh g^{-1} after 100 cycles) of 100 mA g^{-1} with an excellent rate capability. Additionally, at the ultrafast current density corresponding to 2000 mA g^{-1}, a reversible discharge capacity of 444.4 mAh g^{-1} was obtained, and a sustained cycling stability of 89.9% was obtained after 500 cycles. This was mainly ascribed to the novel effects of the 3D interconnected hybrid network as follows: i) desirable receptive capacity of Li ions into the FTO NPs via nanocarbon network; ii) efficient transportation of formed Li ions and electrons via the hybrid network with FTO NP and nanocarbon; iii) prevention of FTO NP pulverization from the CNFs via the nanocarbon network. Thus, a novel hierarchical core/shell heterostructure can offer a potential construction recipe of ultrafast anode material based on an effective synthetic method for practical applications of LIBs.

4. Experimental Section

Unique hierarchical core/shell heterostructures of CNF/3D interconnected hybrid network with nanocarbon and FTO NP (referred as CNF/C-FTO NP) were fabricated via the one-pot process of HUSPD. For the preparation of the CNFs using electrospinning, 10 wt% polyacrylonitrile (PAN, M_w = 150 000, Aldrich) was dissolved in N,N-dimethylformamide (DMF, Aldrich) for 3 h, and the PAN solution was electrospun under a voltage of 13 kV and feeding rate corresponding to 0.03 mL h^{-1}. Subsequently, to synthetize the CNFs (named as bare CNF), the prepared PAN nanofibers were stabilized at 280 °C for 2 h under air, and the carbonization was then performed at 800 °C for 2 h in nitrogen. Next, the FTO precursor solution for the HUSPD was prepared via dissolving 0.68 M tin chloride ($SnCl_4 \cdot 5H_2O$, SAMCHUN) and 1.19 M NH_4F (NH_4F, Aldrich) into deionized (DI) water with 5 vol% ethyl alcohol (C_2H_6O, Duksan). Subsequently, 1 wt% ketjen black (Akzo-Nobel, KB) as a main source for forming nanocarbon network was dispersed into the FTO precursor solution with the assistance of ultrasonic treatment for 1 h. With respect to the HUSPD of the FTO precursor solutions with KB, the droplets were formed by using an ultrasonic atomizer (1.6 MHz) and were then sprayed for 16 min onto the CNFs in a chamber maintained at 420 °C via the N_2 carrier gas with a flow rate of 15 L min^{-1}. This resulted in the formation of CNF/C-FTO NP. For comparison purposes, the FTO NP-coated CNFs (CNF/FTO NP) were prepared via the one-pot process of the HUSPD using the pure FTO precursor solution without KBs.

The chemical bonding states of the samples were analyzed via FTIR spectroscopy (Thermo Fisher Scientific, Nicolet iS50) and X-ray photoelectron spectroscopy (XPS, AXIS ultra-delay line detector equipped with an Al K$_\alpha$ X-ray source, Korea Basic Science Institute, KBSI, Daedeok Headquarters). The crystal structures were traced via X-ray diffractometry analyses (XRD) with Cu K$_\alpha$ radiation between 10° and 90° given a step size of 0.02°. Thermogravimetric analysis (TGA) and differential scanning calorimetry (DSC, DSC-60, Shimadzu) measurement were performed at a heating rate corresponding to 5 °C min^{-1}. The morphology and structure were examined via field-emission scanning electron microscopy (FESEM) and TEM (Gwangju center of KBSI). The Raman spectra was investigated via the laser-excitation wavelength of 532.1 nm. The measurement of energy-dispersive spectrometry (EDS)-mapping was performed to examine the distribution of elements in the sample. The electrical conductivity was measured via a Hall-effect measurement system (Ecopia, HMS-3000). The specific surface area of the samples was characterized from the Brunauer–Emmett–Teller (BET) via nitrogen adsorption and desorption at 77 K.

The measurement of electrochemical performances was performed using coin-type half cells with the prepared samples as the anode, Li metal foil as the cathode, a porous polypropylene membrane as the separator, Cu foil as the current collector, and a 1.0 M LiPF$_6$ solution in a mixture of ethylene carbonate–dimethyl carbonate (1:1) as the electrolyte. The homogenized slurry was prepared by mixing 80 wt% of the samples as the active materials, 1 wt% KB as the conducting material, and 10 wt% polyvinylidene fluoride as the binder in N-methyl-2-pyrrolidinon. The prepared slurry was coated on the Cu foil using a doctor blade and then dried at 100 °C for 12 h. All coin-type half cells were assembled in a glove box filled with high purity argon atmosphere. EIS analysis was performed in the frequency range of 10^5 to 10^{-2} Hz by employing an AC signal of 5 mV. The charging/discharging estimations in the potential range of 0.05–3.00 V (vs Li/Li$^+$) were performed using a cycler system (WonATech Corp., WMPG 3000) in an incubator at 25 °C. The cycling stability was analyzed at up to 100 cycles at current density corresponding to 100 mA g^{-1}. The rate capability was traced at current densities corresponding to 100, 500, 1000, 1500, 2000, and 100 mA g^{-1}. The ultrafast cycling durability was investigated at up to 500 cycles at a high current density corresponding to 2000 mA g^{-1}.

Supporting Information

Supporting Information is available from the Wiley Online Library or from the author.

Conflict of Interest

The authors declare no conflict of interest.

[1] X. Zeng, M. Li, D. A. El-Hady, W. Alshitari, A. S. Al-Bogami, J. Lu, K. Amine, *Adv. Energy Mater.* **2019**, *9*, 1900161.

[2] M. Han, Y. Mu, F. Yuan, J. Liang, T. Jiang, X. Bai, J. Yu, *J. Mater. Chem. A* **2020**, *8*, 3822.

[3] X. Wu, S. Xia, Y. Huang, X. Hu, B. Yuan, S. Chen, Y. Yu, W. Liu, *Adv. Funct. Mater.* **2019**, *29*, 1903961.

[4] H. Kim, H. Kim, S. Muhammad, J. H. Um, M. S. A. S. Shah, P. J. Yoo, W.-S. Yoon, *J. Power Sources* **2020**, *446*, 227321.

[5] S. Wang, L. Shi, G. Chen, C. Ba, Z. Wang, J. Zhu, Y. Zhao, M. Zhang, S. Yuan, *ACS Appl. Mater. Interfaces* **2017**, *9*, 17163.

[6] J. S. Chen, X. W. Lou, *Small* **2013**, *9*, 1877.

[7] X. Zhou, L. Yu, X. W. Lou, *Adv. Energy Mater.* **2016**, *6*, 1600451.

[8] Y. Zhang, L. Wang, H. Xu, J. Cao, D. Chen, W. Han, *Adv. Funct. Mater.* **2020**, *30*, 1909372.

[9] K. Jeong, J.-M. Kim, S. H. Kim, G. Y. Jung, J. Yoo, S.-H. Kim, S. K. Kwak, S.-Y. Lee, *Adv. Funct. Mater.* **2019**, *29*, 1806937.

[10] W. Dong, J. Xu, C. Wang, Y. Lu, X. Liu, X. Wang, X. Yuan, Z. Wang, T. Lin, M. Sui, I.-W. Chen, F. Huang, *Adv. Mater.* **2017**, *29*, 1700136.

[11] X. Wang, X. Cao, L. Bourgeois, H. Guan, S. Chen, Y. Zhong, D.-M. Tang, H. Li, T. Zhai, L. Li, Y. Bando, D. Golberg, *Adv. Funct. Mater.* **2012**, *22*, 2682.

[12] R. Liu, D. Li, C. Wang, N. Li, Q. Li, X. Lü, J. S. Spendelow, G. Wu, *Nano Energy* **2014**, *6*, 73.

[13] C. Dong, W. Dong, Q. Zhang, X. Huang, L. Gu, I.-W. Chen, F. Huang, *J. Mater. Chem. A* **2020**, *8*, 626.

[14] Z Chen, M. Zhou, Y. Cao, X. Ai, H. Yang, J. Liu, *Adv. Energy Mater.* **2012**, *2*, 95.

[15] P. Dou, Z. Cao, C. Wang, J. Zheng, X. Xu, *Chem. Eng. J.* **2017**, *320*, 405.

[16] F. Zoller, K. Peters, P. M. Zehetmaier, P. Zeller, M. Döblinger, T. Bein, Z. Sofer, D. Fattakhova-Rohlfing, *Adv. Funct. Mater.* **2018**, *28*, 1706529.

[17] K. L. Chopra, S. Major, D. K. Pandya, *Thin Solid Films* **1983**, *102*, 1.

[18] B.-R. Koo, M.-H. Jo, K.-H. Kim, H.-J. Ahn, *NPG Asia Mater.* **2020**, *12*, 10.

[19] V. Kumar, A. Govind, R. Nagarajan, *Inorg. Chem.* **2011**, *50*, 5637.

[20] B.-R. Koo, J.-W. Bae, H.-J. Ahn, *Ceram. Int.* **2019**, *45*, 10260.

[21] H.-G. Wang, Q. Wu, Y. Wang, X. Wang, L. Wu, S. Song, H. Zhang, *Adv. Energy Mater.* **2019**, *9*, 1802993.

[22] S. Yang, W. Yue, J. Zhu, Y. Ren, X. Yang, *Adv. Funct. Mater.* **2013**, *23*, 3570.

[23] G.-H. An, D.-Y. Lee, Y.-J. Lee, H.-J. Ahn, *ACS Appl. Mater. Interfaces* **2016**, *8*, 30264.

[24] W. Yao, S. Wu, L. Zhan, Y. Wang, *Chem. Eng. J.* **2019**, *361*, 329.

[25] B.-R. Koo, D.-H. Oh, D.-H. Riu, H.-J. Ahn, *ACS Appl. Mater. Interfaces* **2017**, *9*, 44584.

[26] H. Wang, F. Fu, F. Zhang, H.-E. Wang, S. V. Kershaw, J. Xu, S.-G. Sun, A. L. Rogach, *J. Mater. Chem.* **2012**, *22*, 2140.

[27] A. Facchetti, T. J. Marks, H. E. Katz, J. Veinot, in *Printed Organic and Molecular Electronics* (Eds: D. R. Gamota, P. Brazis, K. Kalyanasundaram, J. Zhang), Kluwer Academic, Boston **2004**, pp. 230–242.

[28] G. B. Darband, M. Aliofkhazraei, S. Khorsand, S. Sokhanvar, A. Kaboli, *Arabian J. Chem.* **2020**, *13*, 1763.

[29] G. I. Razdyakonova, O. A. Kokhanovskaya, V. A. Likholobov, *Proc. Eng.* **2015**, *113*, 43.

[30] S. Kitabayashi, N. Koga, *J. Phys. Chem. C* **2015**, *119*, 16188.

[31] V. S. Marakatti, G. V. Shanbhag, A. B. Halgeri, *RSC Adv.* **2013**, *3*, 10795.

[32] G. Korotcenkov, V. Macsanov, V. Brinzari, V. Tolstoy, J. Schwank, A. Cornet, J. Morante, *Thin Solid Films* **2004**, *467*, 209.

[33] A. Smith, J.-M. Laurent, D. S. Smith, J.-P. Bonnet, R. R. Clemente, *Thin Solid Films* **1995**, *266*, 20.

[34] J. Sun, L. Xiao, S. Jiang, G. Li, Y. Huang, J. Geng, *Chem. Mater.* **2015**, *27*, 4594.

[35] K.-H. Kim, B.-R. Koo, H.-J. Ahn, *Ceram. Int.* **2018**, *44*, 9408.

[36] G. Fang, X. Deng, J. Zou, X. Zeng, *Electrochim. Acta* **2019**, *295*, 498.

[37] R. Sadri, M. Hosseini, S. N. Kazi, S. Bagheri, N. Zubir, K. H. Solangi, T. Zaharinie, A. Badarudin, *J. Colloid Interface Sci.* **2017**, *504*, 115.

[38] M. Dirican, M. Yanilmaz, K. Fu, Y. Lu, H. Kizil, X. Zhang, *J. Power Sources* **2014**, *264*, 240.

[39] W. Gou, X. Kong, Y. Wang, Y. Ai, S. Liang, A. Pan, G. Cao, *Chem. Eng. J.* **2019**, *374*, 545.

[40] C.-M. Chen, Q. Zhang, J.-Q. Huang, W. Zhang, X.-C. Zhao, C.-H. Huang, F. Wei, Y.-G. Yang, M.-Z. Wang, D. S. Su, *J. Mater. Chem.* **2012**, *22*, 13947.

[41] L. Zhang, G. Zhang, H. B. Wu, L. Yu, X. W. Lou, *Adv. Mater.* **2013**, *25*, 2589.

[42] K. M. Jeon, J. S. Cho, Y. C. Kang, *J. Power Sources* **2015**, *295*, 9.

[43] L. Li, A. Kovalchuk, J. M. Tour, *Nano Res.* **2014**, *7*, 1319.

[44] G. Derrien, J. Hassoun, S. Panero, B. Scrosati, *Adv. Mater.* **2007**, *19*, 2336.

[45] W. Wang, Y. Liang, Y. Kang, L. Liu, Z. Xu, X. Tian, W. Mai, H. Fu, H. Lv, K. Teng, X. Jiao, F. Li, *Mater. Chem. Phys.* **2019**, *223*, 762.

[46] Y. Yang, X. Ji, F. Lu, Q. Chen, C. E. Banks, *Phys. Chem. Chem. Phys.* **2013**, *15*, 15098.

[47] J. Zhang, Z. Ma, W. Jiang, Y. Zou, Y. Wang, C. Lu, *J. Electroanal. Chem.* **2016**, *767*, 49.

[48] D. Song, S. Wang, R. Liu, J. Jiang, Y. Jiang, S. Huang, W. Li, Z. Chen, B. Zhao, *Appl. Surf. Sci.* **2019**, *478*, 290.

[49] Q. Tian, Z. Zhang, L. Yang, S.-I. Hirano, *J. Mater. Chem. A* **2014**, *2*, 12881.

[50] H. Zhang, L. Li, Z. Li, W. Zhong, H. Liao, Z. Li, *Appl. Surf. Sci.* **2018**, *442*, 65.

[51] A. Bhaskar, M. Deepa, M. Ramakrishna, T. N. Rao, *J. Phys. Chem. C* **2014**, *118*, 7296.

[52] X. Lu, Q. Mao, Q. Xiong, S. Pan, X. Duan, Z. Ji, *J. Solid State Chem.* **2019**, *277*, 556.

[53] L. Zhou, J. Zhang, Y. Wu, W. Wang, H. Ming, Q. Sun, L. Wang, J. Ming, H. N. Alshareef, *Adv. Energy Mater.* **2019**, *9*, 1902194.

[54] L. Zhou, Z. Cao, W. Wahyudi, J. Zhang, J.-Y. Hwang, Y. Cheng, L. Wang, L. Cavallo, T. Anthopoulos, Y.-K. Sung, H. N. Alshareef, J. Ming, *ACS Energy Lett.* **2020**, *5*, 766.

[55] Y. Fang, X.-Y. Yu, X. W. Lou, *Adv. Mater.* **2018**, *30*, 1706668.

[56] Y. Fang, B. Y. Guan, D. Luan, X. W. Lou, *Small* **2019**, *58*, 7739.

[57] D. Chao, P. Liang, Z. Chen, L. Bai, H. Shen, X. Liu, X. Xia, Y. Zhao, S. V. Savilov, J. Lin, Z. X. Shen, *ACS Nano* **2016**, *10*, 10211.

[58] E. Lim, C. Jo, H. Kim, M.-H. Kim, Y. Mun, J. Chun, Y. Ye, J. Hwang, K.-S. Ha, K. C. Roh, K. Kang, S. Yoon, J. Lee, *ACS Nano* **2015**, *9*, 7497.

[59] X. Li, X. Sun, Z. Gao, X. Hu, J. Guo, S. Cai, R. Guo, H. Ji, C. Zheng, W. Hu, *Appl. Surf. Sci.* **2018**, *433*, 713.

[60] Y. Yang, Z.-Z. Pan, Y.-Y. Wang, Y.-C. Ma, C. Li, Y.-J. Lu, X.-L. Wu, *Nanoscale* **2019**, *11*, 14616.

[61] H.-G. Wang, Q. Wu, Y. Wang, X. Wang, L. Wu, S. Song, H. Zhang, *Adv. Energy Mater.* **2019**, *9*, 1802993.

[62] Y. Jiang, Y. Li, P. Zhou, Z. Lan, Y. Lu, C. Wu, M. Yan, *Adv. Mater.* **2017**, *29*, 1606499.

[63] E. Lim, C. Jo, H. Kim, M.-H. Kim, Y. Mun, J. Chun, Y. Ye, J. Hwang, K.-S. Ha, K. C. Roh, K. Kang, S. Yoon, J. Lee, *ACS Nano* **2015**, *9*, 7497.

[64] E. Lim, C. Jo, M. S. Kim, M.-H. Kim, J. Chun, H. Kim, J. Park, K. C. Roh, K. Kang, S. Yoon, J. Lee, *Adv. Funct. Mater.* **2016**, *26*, 3711.